The Astrophysical Journal Letters, 970:L30 (11pp), 2024 August 1 https://doi.org/10.3847/2041-8213/ad5ffd
© 2024. The Author(s). Published by the American Astronomical Society.
OPEN ACCESS

Discovery of an Extremely *r*-process-enhanced Thin-disk Star with [Eu/H] = +0.78

Xiao-Jin Xie[1,2], Jianrong Shi[1,2,3], Hong-Liang Yan[1,2,4], Tian-Yi Chen[1,2], Carlos Allende Prieto[5,6], Timothy C. Beers[7], Shuai Liu[1], Chun-Qian Li[1,2], Ming-Yi Ding[1,2], Yao-Jia Tang[1,2], Ruizhi Zhang[1,2], and Renjing Xie[1,2]

[1] CAS Key Laboratory of Optical Astronomy, National Astronomical Observatories, Chinese Academy of Science, Beijing 100101, People's Republic of China; sjr@bao.ac.cn
[2] School of Astronomy and Space Science, University of Chinese Academy of Sciences, Beijing 100049, People's Republic of China
[3] School of Physics and Technology, Nantong University, Nantong 226019, People's Republic of China
[4] Institute for Frontiers in Astronomy and Astrophysics, Beijing Normal University, Beijing 102206, People's Republic of China
[5] Instituto de Astrofísica de Canarias, Vía Láctea S/N, E-38205 La Laguna, Tenerife, Spain
[6] Universidad de La Laguna, Departamento de Astrofísica, E-38206 La Laguna, Tenerife, Spain
[7] Department of Physics and JINA Center for the Evolution of the Elements, University of Notre Dame, Notre Dame, IN 46556, USA
Received 2024 June 3; revised 2024 July 5; accepted 2024 July 6; published 2024 July 24

Abstract

Highly *r*-process-enhanced (RPE) stars are rare and usually metal poor ([Fe/H] < -1.0), and they mainly populate the Milky Way halo and dwarf galaxies. This study presents the discovery of a relatively bright ($V = 12.72$), highly RPE (*r*-II) star ([Eu/Fe] $= +1.32$, [Ba/Eu] $= -0.95$), LAMOST J020623.21+494127.9. This star was selected from the Large Sky Area Multi-Object Fiber Spectroscopic Telescope medium-resolution ($R \sim 7500$) spectroscopic survey; follow-up high-resolution ($R \sim 25{,}000$) observations were conducted with the High Optical Resolution Spectrograph installed on the Gran Telescopio Canarias. The stellar parameters ($T_{\rm eff} = 4130$ K, log g $= 1.52$, [Fe/H] $= -0.54$, $\xi = 1.80$ km s^{-1}) have been inferred taking into account nonlocal thermodynamic equilibrium effects. The abundances of [Ce/Fe], [Pr/Fe], and [Nd/Fe] are +0.19, +0.65, and +0.64, respectively, relatively low compared to the Solar *r*-process pattern normalized to Eu. This star has a high metallicity ([Fe/H] $= -0.54$) compared to most other highly RPE stars and has the highest measured abundance ratio of Eu to H ([Eu/H] $= +0.78$). It is classified as a thin-disk star based on its kinematics and does not appear to belong to any known stream or dwarf galaxy.

Unified Astronomy Thesaurus concepts: Stellar abundances (1577); Fundamental parameters of stars (555); Chemically peculiar stars (226)

1. Introduction

The rapid neutron-capture process (*r*-process) is one of the fundamental nucleosynthetic pathways for producing the heaviest elements. Several astrophysical sites have been proposed to satisfy the physical conditions required for the *r*-process, such as core-collapse supernovae (e.g., Sato 1974; Witti et al. 1994; Farouqi et al. 2010; Mirizzi 2015; Tsujimoto 2021), magnetorotational jet-driven supernovae (e.g., Symbalisty et al. 1985; Fujimoto et al. 2008; Nishimura et al. 2015; Obergaulinger et al. 2018; Reichert et al. 2023), common envelop jet supernovae (e.g., Grichener & Soker 2019; Jin & Soker 2023), collapsars (Siegel et al. 2019), and neutron star mergers (NSMs; Lattimer & Schramm 1974; Rosswog et al. 2014; Thielemann et al. 2017). The detection of GW170817 (Abbott et al. 2017) and its electromagnetic counterpart shows that NSMs can indeed produce *r*-process elements (Drout et al. 2017; Kasen et al. 2017; Pian et al. 2017; Watson et al. 2019). Research is still ongoing to determine whether NSMs are the sole source of *r*-process elements; some studies suggest that the observed *r*-process-element abundance patterns require multiple sites (e.g., Côté et al. 2018, 2019; Hotokezaka et al. 2018; Siegel 2019; Brauer et al. 2021; Farouqi et al. 2022; Tsujimoto 2022; Yamazaki et al. 2021; Naidu et al. 2022; Ekanger et al. 2023; Kobayashi et al. 2023).

Generally, *r*-process-enhanced (RPE) stars are metal poor, with [Fe/H] < -1.0 (e.g., McWilliam et al. 1995; Sneden et al. 2008; Holmbeck et al. 2020), and they are mainly restricted to the Milky Way (MW) halo and dwarf galaxies (e.g., Hirai et al. 2015; Ji et al. 2016; Jeon et al. 2021; Matsuno et al. 2021). These stars are classified as *r*-I, *r*-II, or limited-*r*, depending on the level of *r*-process enrichment (Beers & Christlieb 2005; Frebel 2018; Holmbeck et al. 2020). The dominant *r*-process patterns (Ba to Hf) of these stars are nearly identical (sometimes referred to as "universality"), although some star-to-star differences between the lightest and heaviest elements remain (e.g., Sneden et al. 1994; Aoki et al. 2017; Sakari et al. 2018; Roederer et al. 2022a). Information on the elemental abundances and kinematics of these stars constrain their early enrichment history, which is crucial to understanding the origin of the *r*-process.

This work reports on the discovery of an RPE star with [Fe/H] > -0.6 that is kinematically associated with the thin disk of the MW. Section 2 introduces the observations, and Section 3 describes the determination of stellar atmospheric parameters. A detailed abundance analysis and estimates of uncertainties are presented in Section 4. A discussion of the implications of the existence of this star and an old (but uncertain) estimate of its nucleosynthetic age based on the observed [Th/Eu] ratio are provided in Section 5, followed by a summary of our conclusions in Section 6.

2. Observations

The RPE candidate LAMOST J020623.21+494127.9 (hereafter J0206+4941) was selected from the Large Sky Area Multi-Object Fiber Spectroscopic Telescope (LAMOST; Cui et al. 2012; Zhao et al. 2012; Liu et al. 2020; Yan et al. 2022)

Original content from this work may be used under the terms of the Creative Commons Attribution 4.0 licence. Any further distribution of this work must maintain attribution to the author(s) and the title of the work, journal citation and DOI.

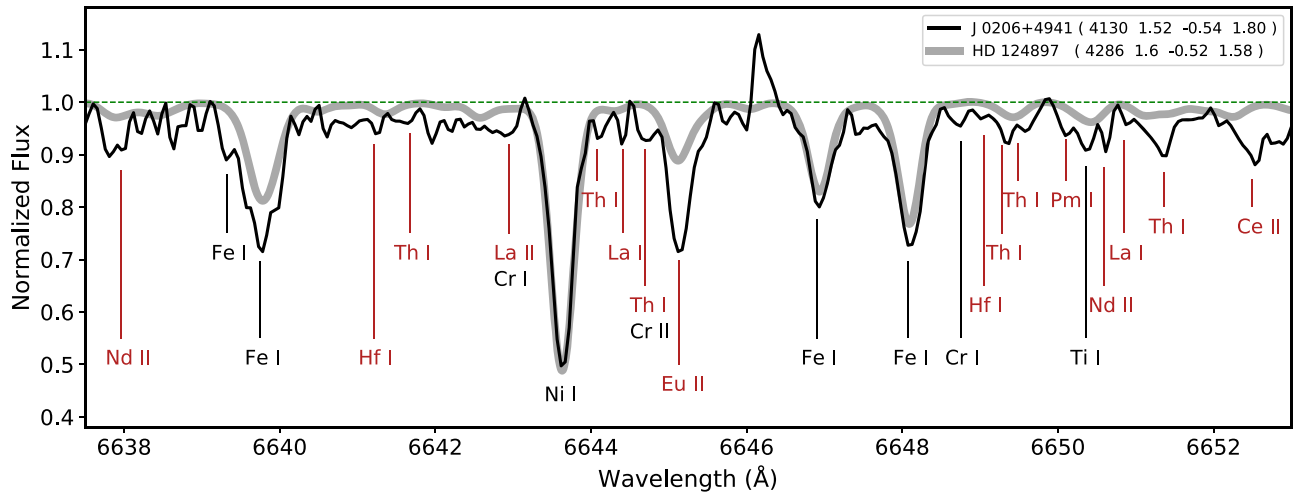

Figure 1. Comparison of high-resolution spectra of J0206+4941 and a moderately RPE (r-I) star, HD 124897 ([Eu/Fe] = +0.45; Forsberg et al. 2019) with similar stellar parameters. The lines of heavy elements are labeled in red, and lines of lighter elements are labeled in black. The stellar parameters ($T_{\rm eff}$, log g, [Fe/H], ξ) are shown in the legend.

Table 1
Target Information

Parameter	Value
Name	LAMOST J020623.21+494127.9
R.A. (J2000)	02:06:23.211
Decl. (J2000)	+49:41:27.914
V mag	12.72 ± 0.24
obsDate$_{\rm LAMOST}$	2018-01-01
obsDate$_{\rm GTC}$	2019-11-18
RV$_{\rm helio}$ (km s^{-1})	-30.86 ± 0.67
Parallax (mas)	0.3106 ± 0.0156[a]
$U_{\rm LSR}$ (km s^{-1})	31.11 ± 0.49
$V_{\rm LSR}$ (km s^{-1})	-11.89 ± 0.50
$W_{\rm LSR}$ (km s^{-1})	9.65 ± 0.35
$r_{\rm apo}$ (kpc)	10.79 ± 0.17
$r_{\rm peri}$ (kpc)	9.68 ± 0.06
$Z_{\rm max}$ (kpc)	0.66 ± 0.03
ecc	0.054 ± 0.004
E (10^3 km^2 s^{-2})	-144.31 ± 0.60
J_r (kpc km s^{-1})	4.82 ± 0.85
J_ϕ (kpc km s^{-1})	2353.05 ± 24.66
J_z (kpc km s^{-1})	8.27 ± 0.51
$T_{\rm eff}$ (K)	4078 ± 100[b]
log g (cgs)	1.62 ± 0.08[b]
$T_{\rm eff}$ (K)	4130 ± 100[c]
log g (cgs)	1.52 ± 0.20[c]
[Fe/H]	-0.54 ± 0.10[c]
$\xi_{\rm t}$(km s^{-1})	1.80 ± 0.20[c]

Notes.
[a] Gaia Collaboration et al. (2023).
[b] Determined by a photometric method.
[c] Determined by a spectroscopic approach.

medium-resolution ($R \sim 7500$) spectroscopic survey by matching the observed spectra to synthetic templates of the region around the Eu II line at 6645.1 Å (Chen et al. 2021). This star is relatively bright ($V < 13$) and substantially more metal rich compared to previously observed r-II stars.

The high-resolution spectrum was taken with the High Optical Resolution Spectrograph (HORuS) installed on the Gran Telescopio Canarias (GTC; Tabernero et al. 2020; Allende Prieto 2021). The spectral wavelength coverage is from 3800 to 6900 Å with a resolving power of $R \sim 25{,}000$. The multiorder echelle spectra were extracted and wavelength calibrated based on Th–Ar hollow-cathode lamp exposures, using the HORuS automated pipeline the `chain`.[8] The signal-to-noise ratio (S/N) at 5600 Å is estimated to be 119 using the code `DER_SNR` (Stoehr et al. 2008). Table 1 lists the basic information of this target, including the details of the observations, kinematics, and stellar atmospheric parameters, as described in detail below.

The high-resolution spectrum of J0206+4941 around 6645 Å is shown in Figure 1, along with the spectrum of HD 124897, a star with similar atmospheric parameters ($T_{\rm eff} = 4286$ K, log $g =$ 1.6 cgs, [Fe/H] = −0.52, and $\xi = 1.58$ km s^{-1}; Blanco-Cuaresma et al. 2014). The slightly higher $T_{\rm eff}$ of HD 124897 leads to stronger Fe-group lines. The lines of heavy elements are labeled in red. HD 124897 has a moderate r-process enhancement of [Eu/Fe] = +0.45 (Forsberg et al. 2019) and is classified as an r-I star. As shown in the figure, the Eu II line of our candidate star is significantly stronger than that of HD 124897. Many lines of heavy elements are weak or absent in the spectra of HD 124897, but they are strong in the spectra of our candidate star, indicating that J0206+4941 has significant r-process enhancement.

3. Stellar Atmospheric Parameters

We first derive initial estimates of the effective temperature and surface gravity of J0206+4941 using a photometric approach. For comparison, we also determine the atmospheric parameters using a spectroscopic approach: effective temperature ($T_{\rm eff}$), surface gravity (log g), metallicity ([Fe/H]), and microturbulent velocity ($\xi_{\rm t}$).

3.1. Photometric Approach

We estimate the effective temperature of our target star based on the photometric color index $(V-K)_0$ with the empirical calibration relations given by Alonso et al. (1999). An adopted reddening $E(B-V)$ of 0.1518 ± 0.0083 is derived using the

[8] The `chain` is written in the Interactive Data Language (IDL), runs in Gnu's Not Unix Data Language, and is available from github.com/callendeprieto/chain.

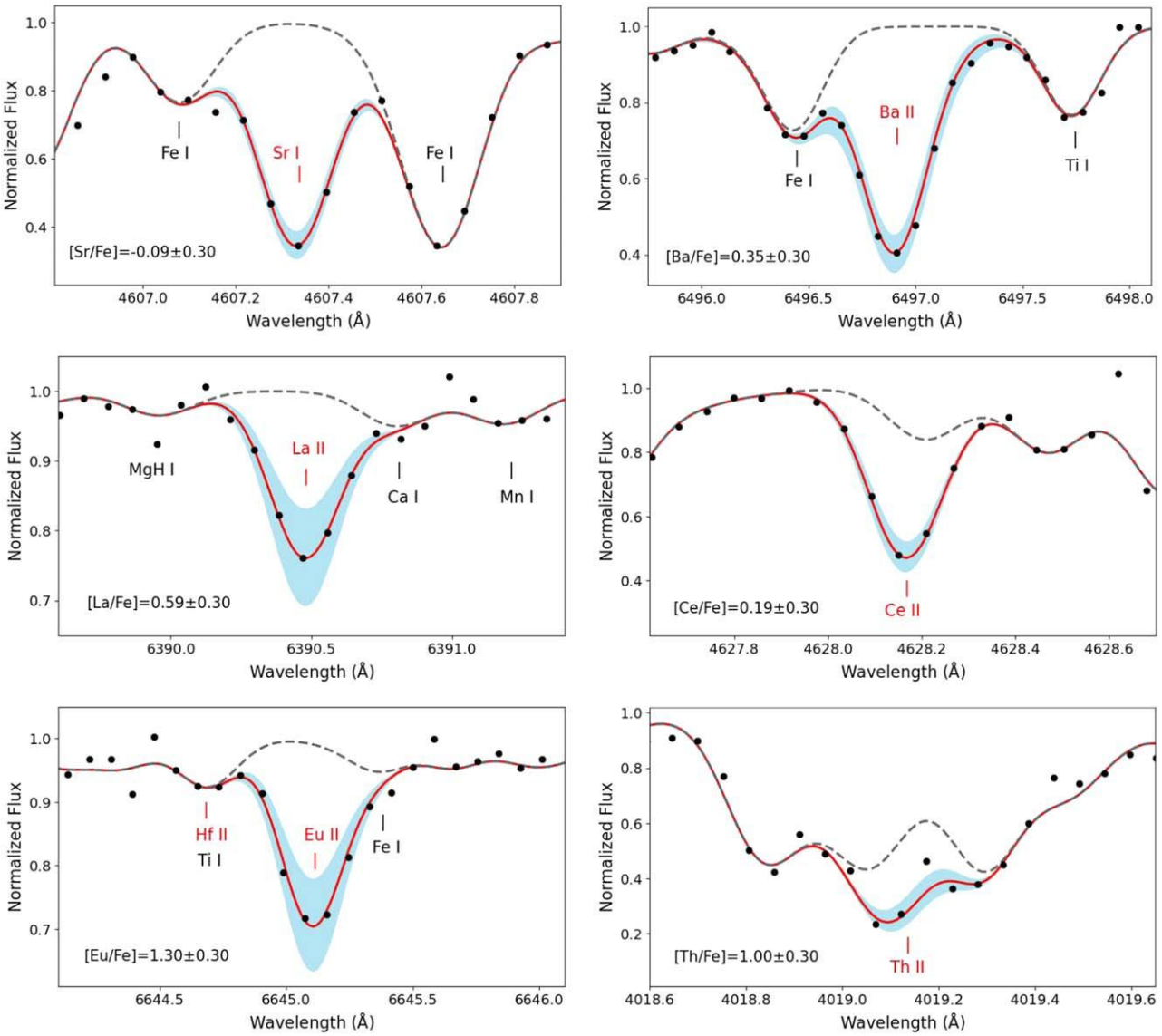

Figure 2. Spectral synthesis for the abundance determinations of Sr, Ba, La, Ce, Eu, and Th. The red line indicates the best-fit synthesis for the line(s) of interest. The blue shaded regions indicate ±0.30 dex deviations from the best fit. The gray dashed lines indicate synthetic spectra in the absence of the element of interest.

GALEXTIN online tool (Amôres et al. 2021) with the Green et al. (2019) 3D dust map. The $E(V-K)$ reddening is determined using the conversions from Ramírez & Meléndez (2005). The surface gravity is calculated using the online code PARAM 1.3 (da Silva et al. 2006), based on the relationships between bolometric flux, temperature, mass, and $\log g$. The calculation requires estimates of $T_{\rm eff}$, [Fe/H], V magnitude, and parallax, where we use [Fe/H] measured by the spectroscopic approach described below, the V magnitude from Zacharias et al. (2013), and the parallax from Gaia DR3 (Gaia Collaboration et al. 2023).

3.2. Spectroscopic Approach

The line list and atomic data of Fe I and Fe II lines are taken from Yan et al. (2018). Only lines with equivalent widths (EWs) between 20 and 120 mÅ, and not heavily blended with other species, have been used. This selection results in 45 Fe I and 7 Fe II lines, respectively. The abundances and EWs of individual Fe lines are analyzed by the interactive IDL code Spectrum Investigation Utility (SIU; Reetz 1999) using the MARCS stellar atmospheric models (Gustafsson et al. 2008). The effects of nonlocal thermodynamic equilibrium (NLTE) are considered specifically for each Fe I line, based on Mashonkina et al. (2011) and following the method described in Sitnova et al. (2015).

A spectroscopic estimate of $T_{\rm eff}$ is obtained from the excitation equilibrium of Fe I lines with excitation energies ($E_{\rm exc}$) higher than 2.0 eV (Sitnova et al. 2015), $\log g$ is estimated from the ionization balance of Fe I and Fe II, and $\xi_{\rm t}$ is obtained by forcing the iron abundances from Fe I lines to be independent of their EWs. We adjust $T_{\rm eff}$, $\log g$, and $\xi_{\rm t}$ by restricting the slope of $\log\epsilon$(Fe I) versus $E_{\rm exc}$ lower than 0.001 dex eV^{-1}, the difference between [Fe II/H] and [Fe I/H] within 0.1 dex, and the slope of $\log\epsilon$(Fe I) versus log(EW) less than 0.01.

The results determined by both methods are listed in Table 1. The difference between the photometric and spectroscopic effective temperatures is only 52 K, and the difference in

Table 2
Elemental Abundances and Uncertainties

Element	N	[X/Fe] LTE	[X/Fe] NLTE	σ_{stat} (dex)	ΔT_{eff} +100 K	$\Delta \log g$ +0.2 dex	Δ[Fe/H] +0.1 dex	$\Delta\xi$ +0.2 km s^{-1}	σ_{sys} (dex)	σ_{Total} (dex)
C (CH)	...	−0.20	...	...	...	...	...	...	...	...
Na I	4	+0.26	+0.05	0.03	0.04	−0.01	0.00	−0.07	0.08	0.11
Mg I	3	+0.31	+0.24	0.02	0.02	−0.02	0.00	−0.06	0.07	0.09
Al I	2	+0.18	+0.08	0.01	0.07	0.01	−0.01	−0.03	0.08	0.09
Si I	3	+0.23	+0.22	0.05	−0.08	0.03	0.01	−0.04	0.09	0.14
Ca I	7	−0.02	−0.04	0.05	0.07	0.00	0.02	−0.09	0.12	0.17
Sc II	4	+0.12	...	0.08	−0.01	0.04	0.02	−0.06	0.08	0.16
Ti II	3	+0.09	+0.08	0.04	−0.03	0.04	0.02	−0.07	0.09	0.13
V I	1	+0.10	...	...	0.02	0.03	0.01	−0.06	0.07	0.07
V II	1	+0.06	...	...	0.02	0.04	0.00	−0.07	0.08	0.08
Cr I	4	−0.02	+0.09	0.02	−0.01	0.04	0.02	−0.06	0.08	0.10
Mn I	3	+0.10	+0.17	0.01	0.03	0.01	0.02	−0.09	0.10	0.11
Co I	1	+0.00	−0.08	...	0.01	0.03	0.01	−0.07	0.08	0.08
Ni I	5	−0.10	...	0.01	0.01	0.03	0.00	−0.06	0.07	0.08
Cu I	3	−0.07	−0.04	0.02	−0.01	0.02	0.01	−0.13	0.13	0.15
Zn I	2	−0.19	...	0.01	0.02	0.02	0.00	−0.10	0.10	0.11
Sr I	1	−0.09	...	...	0.12	0.00	0.00	−0.12	0.17	0.17
Y II	3	+0.41	...	0.05	−0.02	0.04	0.02	−0.01	0.05	0.10
Zr II	3	+0.67	...	0.02	−0.03	0.04	0.03	−0.02	0.06	0.08
Ba II	3	+0.42	+0.37	0.08	0.02	0.03	0.02	−0.12	0.13	0.21
La II	2	+0.57	...	0.03	0.03	0.04	0.03	−0.03	0.07	0.10
Ce II	3	+0.19	...	0.10	0.02	0.02	0.02	−0.09	0.10	0.20
Pr II	2	+0.65	...	0.06	0.03	0.04	0.02	−0.01	0.05	0.11
Nd II	3	+0.64	...	0.03	0.00	0.04	0.01	−0.10	0.11	0.14
Sm II	3	+1.10	...	0.08	0.02	0.03	0.03	−0.07	0.08	0.16
Eu II	2	+1.20	+1.32	0.07	0.00	0.04	0.02	−0.03	0.05	0.12
Gd II	4	+1.14	...	0.18	0.01	0.04	0.02	−0.03	0.05	0.23
Dy II	1	+1.30	...	...	0.02	0.03	0.00	−0.02	0.04	0.04
Lu II	1	+0.20	...	...	−0.02	0.03	0.02	−0.01	0.04	0.04
Hf II	1	+1.10	...	...	−0.02	0.05	0.03	−0.02	0.06	0.06
Th II	1	+1.00	...	...	0.02	0.02	0.03	−0.15	0.16	0.16

surface gravities between the two methods is 0.10 dex. We adopt the spectroscopic parameters in the following analysis.

4. Analysis of Elemental Abundances

4.1. Abundance Estimates

We use a spectrum-synthesis approach for the abundance determination. The line list and atomic data are taken from Zhao et al. (2016) and Roederer et al. (2018b); we have slightly revised the log gf values by fitting the solar spectrum (Kurucz et al. 1984). The influence of hyperfine structure is considered for Sc (Zhang et al. 2008), Cu (Shi et al. 2014), Sr (Borghs et al. 1983), Ba (Kurucz & Bell 1995), and Eu (Lawler et al. 2001). We calculate the theoretical line profiles by SIU, using the MARCS stellar model atmospheres (Gustafsson et al. 2008). The solar abundances are adopted from Asplund et al. (2009).

The carbon abundance is estimated from the molecular CH G-band region around 4310 Å; the line list we adopted comes from Masseron et al. (2014). Among the light odd-Z elements, we can obtain abundance estimates of Na and Al. Four Na I lines at 5682, 5688, 6154, and 6160 Å and two Al I lines at 6696 and 6698 Å have been used. The α-elements with detectable lines include Mg, Si, Ca, and Ti, while the [O I] line at 6300 Å is too weak to derive a reliable abundance. NLTE effects have been taken into consideration, based on Gehren et al. (2004; Na), Baumueller & Gehren (1996; Al), Mashonkina (2013; Mg), Shi et al. (2008; Si), Mashonkina et al. (2007; Ca), Sitnova et al. (2016; Ti), and Shi et al. (2014; Cu). In addition, the NLTE corrections for lines of Cr I, Mn I, and Co I are obtained from an online spectral tool.[9]

The neutron-capture elements frequently have their absorption lines blended with other elements. This is especially the case for relatively metal-rich stars, as strong Fe lines often lead to strong blends. Figure 2 shows a sample of spectral synthesis for the Sr I, Ba II, La II, Ce II, Eu II, and Th II lines. We use the Sr I line at 4607 Å to determine the Sr abundance. There are numerous very strong absorption lines for elements such as Fe and Ti lines around 4077 and 4161 Å, making it difficult to distinguish the absorption lines of Sr II. The abundance of Ba is derived from the Ba II lines at 4554, 4934, 6141, and 6496 Å. The NLTE effects have been taken into account (Mashonkina et al. 1999). The abundance of Eu is derived from the Eu II lines at 4129, 4205, 6049, and 6645 Å, with the NLTE effects considered (Mashonkina & Gehren 2000). As the lines at 4129 and 4205 Å are heavily blended, only upper limits on Eu are obtained from these two lines. The abundance of Ce is derived from the Ce II lines at 4418, 4628, and 5247 Å. The abundance of Th is estimated by using the Th II line at 4019 Å. The abundances for a total of 15 neutron-capture elements, namely, Sr, Y, Zr, Ba, La, Ce, Pr, Nd, Sm, Eu, Gd, Dy, Lu, Hf, and Th, have been determined; the results are listed in Table 2.

[9] https://nlte.mpia.de (Kovalev 2019).

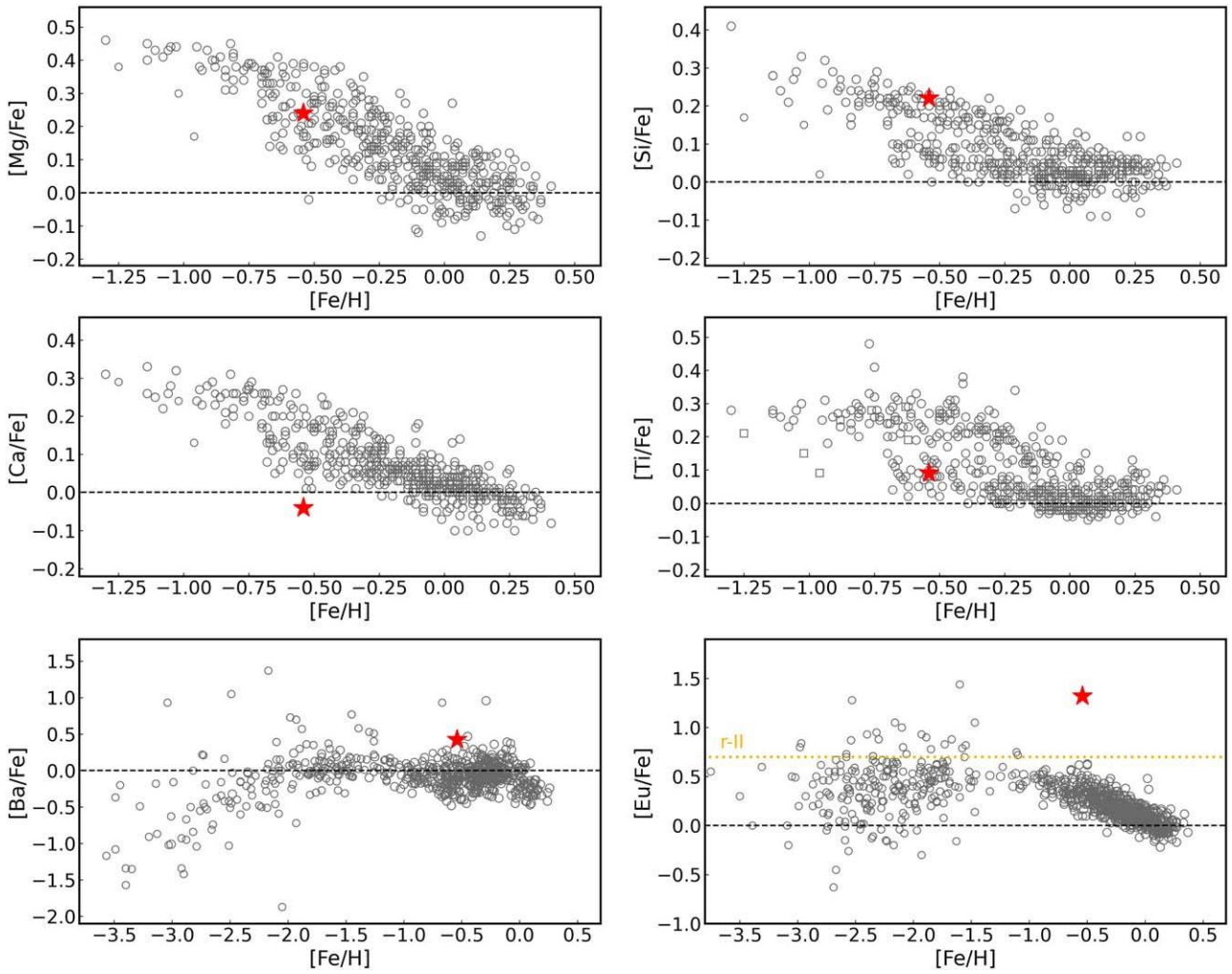

Figure 3. Comparison of abundance ratios in J0206+4941 (red star) with MW field stars (gray circles). The abundance ratios of the MW stars come from Venn et al. (2004), Bensby et al. (2014), Battistini & Bensby (2016), Forsberg et al. (2019), and Holmbeck et al. (2020). The black dashed line is the solar reference line. The orange dashed line in the [Eu/Fe] vs. [Fe/H] panel indicates the *r*-II limit (+0.7) as defined by Holmbeck et al. (2020).

4.2. Uncertainties

To estimate the uncertainty of the abundance determinations, two types of error sources are considered: systematic errors ($\sigma_{\rm sys}$, due to errors in the stellar atmospheric parameters) and statistical errors ($\sigma_{\rm stat}$, due to the line measurements themselves). Table 2 lists the abundance differences when changing $T_{\rm eff}$ by +100 K, log g by +0.2 dex, [Fe/H] by +0.1 dex, and $\xi_{\rm t}$ by +0.2 km s^{-1}. The $\sigma_{\rm sys}$ is calculated by taking the square root of the quadratic sum of the errors associated with the atmospheric parameters. The $\sigma_{\rm stat}$ is the line-to-line dispersion divided by $\sqrt{N}$, where N is the number of lines used for a given element. Finally, we computed the total error, represented as $\sigma_{\rm Total}$, by summing $\sigma_{\rm sys}$ and $\sigma_{\rm stat}$ in quadrature.

5. Discussion

5.1. The Light and Fe-peak Elements

The observed carbon abundance of J0206+4941 is deficient relative to the solar value ([C/Fe] = −0.20). However, this star falls in the red giant region; therefore, its carbon has been depleted during the normal course of giant branch evolution. Using the procedure described by Placco et al. (2014), the carbon depletion for J0206+4941 is ∼0.2 dex, yielding a natal [C/Fe] ≈ 0.00, indicating that this star was likely never C enhanced. From inspection of Figure 3, the abundances of Mg, Si, and Ti appear similar to those of the MW field stars. Although the [Ca/Fe] ratio is slightly lower, it is still close to the boundary of other field stars. The [Na/Fe] and [Al/Fe] ratios (not shown in the figure) are both slightly supersolar.

Among the Fe-group elements, [V/Fe], [Cr/Fe], and [Mn/Fe] are slightly overabundant, while [Co/Fe], [Ni/Fe], [Cu/Fe], and [Zn/Fe] are slightly underabundant. All of these abundance ratios are normal compared to stars of similar metallicity (e.g., Battistini & Bensby 2015).

5.2. The r-process Enhancement and Pattern

The lower two panels of Figure 3 show the [Ba/Fe] and [Eu/Fe] ratios of J0206+4941 compared to MW field stars. From inspection, this star exhibits a very strong enhancement of [Eu/Fe] (+1.32) and a slight enhancement of [Ba/Fe] (+0.37). The low [Ba/Eu] ratio (−0.95) indicates that its neutron-capture elements are mainly due to the *r*-process.

In order to put J0206+4941 in the context of other highly RPE stars, we have listed the known RPE stars with [Eu/Fe] ⩾ +1.0 in Table A1, ordered by decreasing [Eu/H]. As shown in this table, most of these stars have low metallicity ([Fe/H] < −1.0)

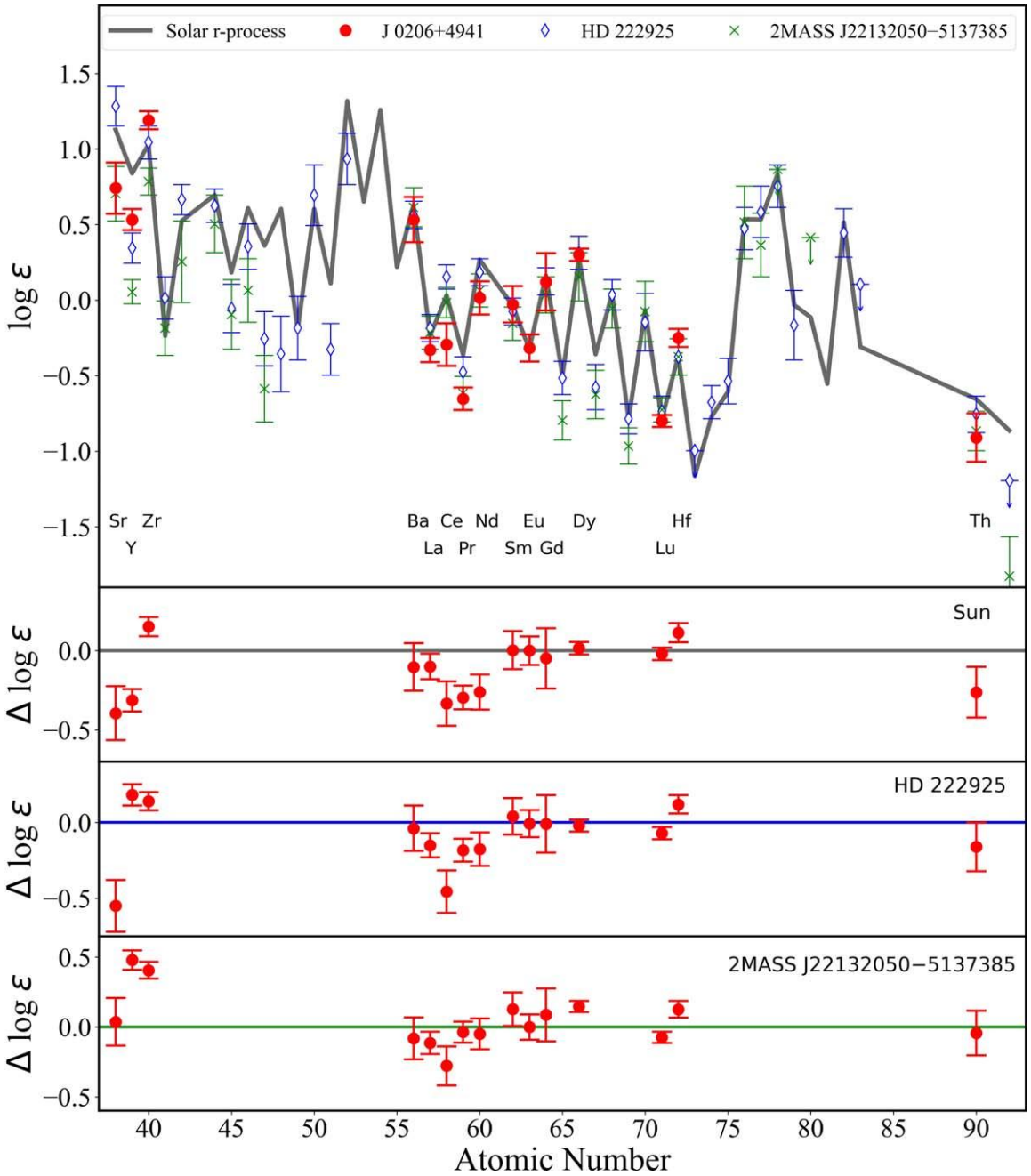

Figure 4. The heavy-element abundances of J0206+4941 are shown in the top panel, with the solar *r*-process pattern, abundances of HD 222925 (Roederer et al. 2022b), and 2MASS J22132050-5137385 (Roederer et al. 2024) normalized to match the Eu abundance of J0206+4941. Residuals between J0206+4941 and the solar *r*-process pattern, HD 222925, and 2MASS J22132050-5137385 are shown in the lower panels.

and are identified as members of the MW halo, while a a few such stars are found in dwarf galaxies or globular clusters. J0206 +4941 is the first strongly RPE star associated with the MW disk and has a relatively high metallicity ($[Fe/H] = -0.54$). The [Eu/H] of J0206+4941 is +0.78, which is the highest among known RPE stars.

Many previous studies have found that the main *r*-process abundance patterns of metal-poor RPE stars are very close to that of the solar *r*-process. This agreement is most noticeable for the elements from Ba to Hf, although there are some differences in light neutron-capture elements (e.g., Sneden et al. 1994; Roederer et al. 2014b; Sakari et al. 2018) and star-to-star variations among the actinides. A comparison of the heavy-element abundances in J0206+4941 with the solar *r*-process and two RPE "template" stars (HD 222925, Roederer et al. 2022b; 2MASS J22132050-5137385, Roederer et al. 2024) is shown in the top panel of Figure 4, where the solar *r*-process, HD 222925, and 2MASS J22132050-5137385 *r*-process patterns are normalized to the Eu abundance of J0206+4941. The residuals are presented in the bottom panels.

The abundance pattern of J0206+4941 is not perfectly consistent with the solar *r*-process. The elements Sr, Y, Ce, Pr, and Nd are significantly lower compared to the solar pattern, while only Sr and Ce are significantly lower compared to that of HD 222925. When compared to 2MASS J22132050-5137385, the Ce abundance remains lower, and the Y and Zr

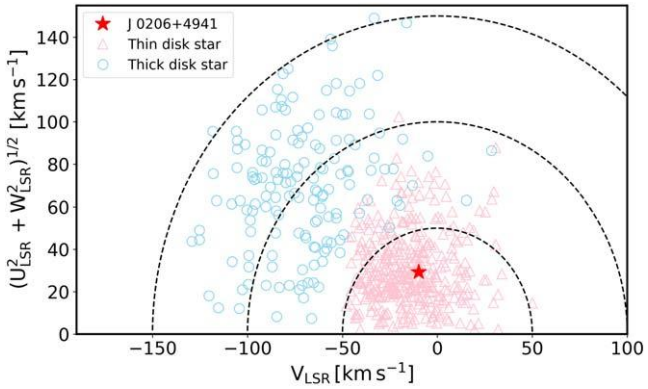

Figure 5. Toomre diagram for J0206+4941. The MW thin-disk stars (pink triangles) and thick-disk stars (blue circles) are from Bensby et al. (2003) and Venn et al. (2004), respectively.

are higher. This difference suggests that the production of *r*-process elements may require multiple sites or multiple mechanisms or that this star's abundances have a different contribution for these elements.

5.3. Kinematics

We measure the heliocentric radial velocity ($RV_{helio} = -30.86 \pm 0.67$ km s^{-1}) from the high-resolution GTC spectrum; it shows no obvious variation from the LAMOST DR7 (-30.94 ± 1.00 km s^{-1}; Luo et al. 2022) and the Gaia DR3 measurements (-30.00 ± 0.40 km s^{-1}; Gaia Collaboration et al. 2023). As a result, J0206+4941 is not likely to be in a binary system.

We calculate the local standard of rest (LSR) Galactic space velocities (U_{LSR}, V_{LSR}, W_{LSR}) for J0206+4941, adopting the coordinates, proper motions, and parallax with zero-point offset corrected[10] from the Gaia DR3 catalog (Gaia Collaboration et al. 2023), as well as the radial velocity derived from the GTC spectrum. The distance derived from the corrected parallax is $d = 3.072 \pm 0.148$ kpc, which is consistent with the photogeometric distance from Bailer-Jones et al. (2021; $d = 3.128 \pm 0.151$ kpc). We use a right-handed Galactocentric Cartesian coordinate system and assume that the Sun is located at ($X_\odot$, $Y_\odot$, $Z_\odot$) = (−8.2, 0.0, 0.0208) kpc (McMillan 2017; Bennett & Bovy 2019), the circular velocity at the solar position is $v_0 = 232.8$ km s^{-1} (McMillan 2017), and the solar peculiar motion is ($U_\odot$, $V_\odot$, $W_\odot$) = (11.1, 12.24, 7.25) km s^{-1} (Schönrich et al. 2010). We adopt the MW potential from McMillan (2017) and employ the `AGAMA` routine (Vasiliev 2019) to derive the orbital energy (E), three-dimensional action ($J = (J_r, J_\phi, J_z)$), pericentric radius (r_{peri}), apocentric radius (r_{apo}), maximum height from the Galactic midplane (Z_{max}), and eccentricity ($ecc = \frac{r_{apo} - r_{peri}}{r_{apo} + r_{peri}}$). We assume Gaussian distributions for its observables and additionally account for the correlated observational uncertainties in proper motions and parallax. We run a Monte Carlo resampling procedure based on 100,000 draws to estimate the uncertainties of the dynamical parameters.

J0206+4941 exhibits typical thin-disk velocities (see Figure 5) with a very low orbital eccentricity ($ecc = 0.054 \pm 0.004$) and limited orbital height ($Z_{max} = 0.66 \pm 0.03$ kpc). Many previously discovered highly RPE stars have accretion origin (e.g., Roederer et al. 2018a; Sakari et al. 2019; Xing et al. 2019). However, J0206+4941 does not appear to be clustered in dynamical phase space with any known accreted structures (Naidu et al. 2020; Reichert et al. 2021; Hattori et al. 2023; Shank et al. 2023); thus, it may well have been formed in situ in the MW's thin disk. This star may have formed from interstellar matter enriched in *r*-process elements by a single binary NSM and/or CCSNe, indicating that mixing may not be isotropic, even in the thin disk. We also note that Hirai et al. (2022) found, in their simulation of the origin of RPE stars in an MW-like galaxy, that all simulated *r*-II stars with [Fe/H] > -1 were formed in situ rather than via accretion from a parent dwarf satellite.

5.4. Age Estimation

The presence of the radioactive element Th allows us to estimate the age of this star, albeit with a large error bar. The age can be estimated using the following relation (Cayrel et al. 2001):

$$t = 46.67\ \mathrm{Gyr}\ [\log \epsilon(\mathrm{Th/Eu})_0 - \log \epsilon(\mathrm{Th/Eu})_{obs}],$$

where $\log \epsilon(\mathrm{Th/Eu})_0$ is the initial production ratio (PR) corresponding to the element formation at $t = 0$, and $\log \epsilon(\mathrm{Th/Eu})_{obs}$ is the observed ratio after the radioactive element Th has decayed within a time t. We adopted an initial PR from Schatz et al. (2002), and the calculated age is 12.32 Gyr. The uncertainty is estimated only from the propagation of the abundance measurement uncertainty. Only one Th line can be measured, and the Th abundance has a systematic error of 0.16 dex, which leads to a large age uncertainty of 9.08 Gyr.

6. Conclusions

We describe the discovery of an extremely RPE thin-disk star, J0206+4941. It was originally selected from the LAMOST medium-resolution survey as a candidate RPE star, based on its unusually strong lines of Eu. A high-S/N, moderately high-resolution ($R \sim 25{,}000$) follow-up observation was obtained using HORuS on the GTC. We derive the abundances of 30 elements and determine the star's kinematics. Our main findings can be summarized as follows:

1. J0206+4941 is the most metal-rich ([Fe/H] = −0.54) highly RPE star found to date and exhibits the highest known abundance ratio of the *r*-process element Eu relative to H ([Eu/H] = +0.78).
2. The abundances of the light elements in this star with $Z \leqslant 30$ are commensurate with other stars of similar metallicity and evolutionary phase, with a strong enhancement of Eu ([Eu/Fe] = +1.32) and modest enhancement of Ba ([Ba/Fe] = +0.37). The observed [Ba/Eu] ratio ([Ba/Eu] = −0.95) indicates that there is relatively little contribution from the *s*-process to the enrichment of the neutron-capture elements.
3. The abundance pattern of the elements with $Z \geqslant 30$ is not perfectly consistent with the scaled solar *r*-process pattern, as demonstrated by the lower abundances of Ce, Pr, and Nd. This difference provides some support for multiple origins of the *r*-process.

[10] The zero-point offset of the parallax is −0.014856 mas, as obtained using the package from https://gitlab.com/icc-ub/public/gaiadr3_zeropoint (Lindegren et al. 2021).

4. J0206+4941 does not exhibit significant radial-velocity variations, indicating it is not likely to be in a binary system.
5. The Galactic space velocities and orbital parameters show that J0206+4941 is restricted to the thin disk of the MW and apparently was not accreted from an external dwarf galaxy.
6. The presence of the radioactive element Th allows us to estimate the age of J0206+4941 as 12.32 ± 9.08 Gyr.

Clearly, a higher-resolution ($R > 50{,}000$) spectrum of this star with better S/N in the blue region would prove illuminating and enable the measurement of numerous other *r*-process elemental abundances, possibly including uranium, enabling derivation of a more accurate age estimate. In addition to J0206+4941, we have also found a few other candidate RPE stars with [Fe/H] > -1.0 from the LAMOST-MRS spectra. These stars are excellent candidates for high-resolution follow-up spectroscopic observations with HORuS and other instruments in the near future.

Acknowledgments

We thank the anonymous referee for valuable suggestions that have improved the manuscript. This research is supported by the National Natural Science Foundation of China under grant Nos. 12090040, 12090044, 12373036, 12022304, and 11973052; the National Key R&D Program of China under grant No. 2019YFA0405502; the Scientific Instrument Developing Project of the Chinese Academy of Sciences under grant No. ZDKYYQ20220009; and the International Partnership Program of the Chinese Academy of Sciences under grant No. 178GJHZ2022047GC. H.-L.Y. acknowledges the support from the Youth Innovation Promotion Association, Chinese Academy of Sciences. C.A.P. is thankful for financial support from the Spanish Ministry MICINN projects AYA2017-86389-P and PID2020-117493GB-I00. T.C.B. acknowledges support from grant PHY 14-30152 (Physics Frontier Center/JINA Center for the Evolution of the Elements (JINA-CEE)) and from OISE-1927130: The International Research Network for Nuclear Astrophysics (IReNA), awarded by the US National Science Foundation.

This Letter is based on observations made with the Gran Telescopio Canarias (GTC), installed at the Spanish Observatorio del Roque de los Muchachos of the Instituto de Astrofísica de Canarias on the island of La Palma. The Guoshoujing Telescope (the Large Sky Area Multi-Object Fiber Spectroscopic Telescope LAMOST) is a National Major Scientific Project built by the Chinese Academy of Sciences. Funding for the project has been provided by the National Development and Reform Commission. LAMOST is operated and managed by the National Astronomical Observatories, Chinese Academy of Sciences.

Appendix

In Table A1, we assemble a list of highly RPE stars, chosen to have [Eu/Fe] $\geqslant +1.0$, sorted by decreasing [Eu/H]. Note that the abundances listed in the table are LTE results. The [C/Fe] listed is the "as measured" quantity, not including corrections for evolutionary state. The column labeled LOC indicates the likely stellar population with which each star is associated.

Table A1
Highly RPE Stars ([Eu/Fe] $\geqslant +1.0$ and [Ba/Eu] < 0.0)

Stellar ID	$T_{\rm eff}$ (K)	log g (cgs)	$\xi_{\rm t}$ (km s^{-1})	[Fe/H]	[Eu/H]	[Eu/Fe]	[Ba/Eu]	[C/Fe]	[Mg/Fe]	LOC	References
LAMOST J020623.21+494127.9	4130	1.52	1.80	−0.54	+0.78	+1.32	−0.95	−0.20	+0.31	Disk	this work
[LDH2014] Fnx-mem0556	4176	0.70	...	−0.79	+0.46	+1.25	−0.88	⋯	−0.15	Fnx[a]	REI21
[LDH2014] Fnx-mem0595	4223	0.66	...	−0.92	+0.46	+1.38	−0.85	⋯	−0.17	Fnx[a]	REI21
BPS CS 31070-073	6190	3.86	1.50	−2.55	+0.28	+2.83	−0.41	+1.34	+0.64	Halo	ALL12
2MASS J22132050-5137385	5509	2.28	1.25	−2.20	+0.25	+2.45	−0.73	+0.38	+0.49	Halo	ROE24
[LDH2014] Fnx-mem0546	4367	0.82	...	−1.33	+0.12	+1.45	−1.05	⋯	−0.11	Fnx[a]	REI21
BPS CS 29526-110	6650	3.79	2.10	−2.19	+0.09	+2.28	−0.01	+2.38	+0.22	Halo	ALL12
UMi COS 92	4325	0.30	1.95	−1.45	+0.04	+1.49	−0.72	⋯	+0.02	UMi[b]	SHE01
HD 222925	5636	2.54	2.20	−1.47	−0.14	+1.33	−0.78	−0.20	+0.41	Halo	ROE18
2MASS J07202253-3358518	5040	2.22	1.78	−1.60	−0.16	+1.44	−0.76	+0.11	⋯	Halo	HOL20
LAMOST J112456.61+453531.3	5180	2.70	1.50	−1.27	−0.17	+1.10	−0.86	−0.41	−0.31	Halo	XIN19
RAVE J040618.2-030525	5260	2.75	1.80	−1.34	−0.17	+1.17	−0.19	+0.54	⋯	Halo	RAS20
DES J033457.57-540531.4	5328	2.85	1.50	−2.08	−0.31	+1.77	−0.41	...	...	Ret II[c]	JI16
2MASS J07103110-7121522	5167	2.94	1.75	−1.47	−0.42	+1.05	−0.72	0.00	⋯	Halo	HOL20
SMSS J175046.30-425506.9	4752	1.55	2.05	−2.17	−0.42	+1.75	−0.90	−0.12	+0.24	Halo	JAC15
RAVEJ153830.9-180424	4995	2.00	1.85	−2.02	−0.50	+1.52	−0.80	+0.12	...	Halo	RAS20
2MASS J18024226-4404426	4701	1.60	2.17	−1.55	−0.50	+1.05	−0.10	+0.35	⋯	Halo	HAN18
2MASS J15213995-3538094	5850	2.10	2.65	−2.80	−0.57	+2.23	−0.88	+0.56	+0.37	Halo	CAI20
SMSS J183128.71-341018.4	4940	2.15	2.00	−1.83	−0.58	+1.25	−0.72	+0.01	+0.22	Bulge	HOW16
2MASS J19570805+5529491	5070	1.30	2.18	−1.72	−0.61	+1.11	−1.26	⋯	+0.31	Halo	HAW18
2MASS J07114252-3432368	4767	1.33	1.74	−1.96	−0.66	+1.30	−0.80	+0.47	+0.31	Halo	SAK18
SMSS J183225.29-334938.4	5293	2.35	1.80	−1.74	−0.66	+1.08	−0.58	−0.22	+0.42	Bulge	HOW16
2MASS J05241392-0336543	4430	2.25	3.00	−2.20	−0.70	+1.50	−1.03	−0.40	−0.14	Halo	EZZ20
2MASS J03073894-0502491	4360	1.75	2.90	−1.98	−0.71	+1.27	−1.13	−0.57	+0.09	Halo	EZZ20
2MASS J13052137-1137220	4600	1.80	2.20	−1.82	−0.73	+1.09	−0.89	−0.30	−0.59	Halo	EZZ20
2MASS J20093393-3410273	4690	1.64	1.70	−2.10	−0.78	+1.32	−1.09	−0.86	⋯	Halo	HAN18
2MASS J00101758-1735387	5200	3.00	1.70	−2.19	−0.84	+1.35	−0.92	0.00	−0.56	Halo	EZZ20
2MASS J12170829+0415146	4540	1.65	2.90	−2.00	−0.90	+1.10	−0.95	−0.40	−0.18	Halo	EZZ20
2MASS J23362202-5607498	4630	1.28	2.15	−2.06	−0.92	+1.14	−0.90	−0.05	⋯	Halo	HAN18
2MASS J00512646-1053170	6440	4.02	1.59	−2.34	−0.97	+1.37	−0.72	+0.62	+0.45	Halo	SHA24

Table A1
(Continued)

Stellar ID	$T_{\rm eff}$ (K)	log g (cgs)	$\xi_{\rm t}$ (km s^{-1})	[Fe/H]	[Eu/H]	[Eu/Fe]	[Ba/Eu]	[C/Fe]	[Mg/Fe]	LOC	References
RAVE J012931.1-160046	4959	1.70	2.65	−2.77	−0.97	+1.80	−0.60	+0.44	+0.47	Halo	RAS20
2MASS J14534137+0040467	4550	1.55	2.30	−2.82	−1.02	+1.80	−0.75	−0.41	+0.92	Halo	EZZ20
DES J033537.06-540401.2	5170	2.45	1.55	−2.73	−1.03	+1.70	−0.30	⋯	⋯	Ret II[c]	JI16
DES J033447.93-540525.0	4900	1.70	1.90	−2.91	−1.04	+1.87	−0.79	⋯	⋯	Ret II[c]	JI16
HE 0048-1109	6265	3.80	1.45	−2.35	−1.06	+1.29	−0.67	+0.61	+0.30	Halo	GUL21
CS 31082-001	4827	1.65	1.70	−2.79	−1.07	+1.72	−0.50	+0.04	+0.46	Halo	SAK18
2MASS J03270229+0132322	5100	2.95	1.80	−2.17	−1.10	+1.07	−0.57	+0.35	+0.07	Halo	EZZ20
HE 0007-1752	5215	2.65	1.45	−2.36	−1.11	+1.25	−0.65	−0.29	−0.33	Halo	GUL21
2MASS J03422816-6500355	4976	2.29	2.05	−2.16	−1.11	+1.05	−0.65	+0.05	⋯	Halo	HOL20
2MASS J15260106-0911388	4499	0.76	2.41	−2.83	−1.13	+1.70	−1.01	−0.82	⋯	Halo	HAN18
DES J033556.28-540316.3	5305	2.95	1.65	−3.54	−1.14	<+2.40	−2.30	⋯	⋯	Ret II[c]	JI16
2MASS J21091825-1310062	4855	1.42	2.10	−2.40	−1.15	+1.25	−1.13	−0.28	⋯	Halo	HAN18
J0246-1518	4948	1.93	1.56	−2.45	−1.16	+1.29	−0.64	−0.07	+0.13	Halo	SAK18
2MASS J14325334-4125494	5020	2.39	1.80	−2.79	−1.18	+1.61	−0.90	−0.14	⋯	Halo	HAN18
CS 29497-004	5013	2.23	1.62	−2.81	−1.19	+1.62	−0.41	+0.22	+0.31	Halo	BAR05
HE 0324-0122	5145	2.45	1.65	−2.41	−1.20	+1.21	−0.75	+0.37	+0.36	Halo	GUL21
2MASS J22182082-3827554	5000	2.70	1.60	−2.32	−1.22	+1.10	−0.60	+0.30	+0.18	Halo	EZZ20
DES J033607.74-540235.5	4833	1.55	2.15	−2.97	−1.23	+1.74	−0.83	⋯	⋯	Ret II[c]	JI16
2MASS J05383296-5904280	5824	2.03	2.84	−2.53	−1.25	+1.28	−0.52	< +0.80	⋯	Halo	HOL20
2MASS J02462013-1518419	4879	1.80	2.35	−2.71	−1.26	+1.45	−0.85	+0.04	⋯	Halo	HAN18
HE 1523-0901	4290	0.20	2.13	−3.09	−1.27	+1.82	−2.37	+0.39	+0.47	Halo	SAK18
2MASS J19161821-5544454	4450	0.65	2.50	−2.35	−1.27	+1.08	−1.20	−0.80	⋯	Halo	HAN18
RAVE J203843.2-002333	4630	1.20	2.15	−2.91	−1.27	+1.64	−0.81	−0.44	+0.36	Halo	PLA17
DES J033523.85-540407.5	4608	1.00	2.40	−3.01	−1.33	+1.68	−0.89	⋯	⋯	Ret II[c]	JI16
2MASS J17225742-7123000	5080	2.67	0.70	−2.42	−1.35	+1.07	−0.37	−0.33	⋯	Halo	HAN18
M15 31914	4338	0.58	2.20	−2.41	−1.35	+1.06	−0.70	⋯	⋯	M15[d]	GAR24
HE 1226-1149	5120	2.35	1.50	−2.91	−1.36	+1.55	−0.65	+0.42	+0.32	Halo	COH13
2MASS J02165716-7547064	4543	0.71	2.44	−2.50	−1.38	+1.12	−0.87	−0.33	...	Halo	HAN18
2MASS J21064294-6828266	5186	2.70	2.90	−2.76	−1.44	+1.32	−0.80	+0.53	⋯	Halo	HAN18
SMSS J175738.37-454823.5	4617	1.20	2.30	−2.46	−1.44	+1.02	−3.01	−0.43	+0.39	Halo	JAC15
SDSS J235718.91-005247.8	5000	4.80	0.00	−3.36	−1.44	+1.92	−0.80	+0.43	+0.19	Halo	AOK10
BPS CS 22892-052	4800	1.50	1.95	−3.10	−1.46	+1.64	−0.65	+0.88	+0.30	Halo	SNE03
SMSS J155430.57-263904.8	4783	1.20	2.20	−2.61	−1.47	+1.14	−0.34	−0.26	+0.33	Halo	JAC15
HE 2224+0143	5198	2.66	1.67	−2.58	−1.53	+1.05	−0.46	+0.35	+0.32	Halo	BAR05
HE 0430-4901	5296	3.12	1.32	−2.72	−1.56	+1.16	−0.66	+0.09	+0.17	Halo	BAR05
HE 1219-0312	5060	2.30	1.60	−2.96	−1.58	+1.38	−0.73	+0.03	+0.41	Halo	HAY09
BPS CS 22958-052	6090	3.75	1.95	−2.62	−1.62	+1.00	−1.00	+0.32	⋯	Halo	ROE14
BPS CS 31078-018	5257	2.75	1.50	−2.85	−1.62	+1.23	−0.51	+0.37	+0.42	Halo	LAI08
HE 1127-1143	5224	2.64	1.59	−2.73	−1.65	+1.08	−0.45	+0.54	+0.22	Halo	BAR05
SMSS J062609.83-590503.2	4960	1.75	1.75	−2.77	−1.71	+1.06	−0.22	+0.27	+0.24	Halo	JAC15
HE 2327-5642	5048	2.22	1.69	−2.95	−1.73	+1.22	−0.56	+0.43	+0.14	Halo	BAR05
CS 29491-069	5103	2.45	1.54	−2.81	−1.75	+1.06	−0.72	+0.18	+0.28	Halo	BAR05
BPS CS 22945-017	6080	3.70	1.25	−2.89	−1.76	+1.13	−0.64	+1.78	⋯	Halo	ROE14
DES J033531.13-540148.2	4925	1.90	1.80	−3.34	−1.84	<+1.50	−2.30	⋯	⋯	Ret II[c]	JI16
BPS CS 22945-058	5990	3.65	1.55	−2.98	−1.84	+1.14	−0.85	+0.68	⋯	Halo	ROE14
HE 0432-0923	5131	2.64	1.54	−3.19	−1.94	+1.25	−0.53	+0.24	+0.34	Halo	BAR05
BPS BS 16929-005	5250	3.10	2.30	−3.15	−2.14	+1.01	−0.74	+1.50	+0.49	Halo	ALL12
SPLUS J142445.34-254247.1	4762	1.58	1.60	−3.82	−2.20	+1.62	−0.37	−0.21	+0.54	Halo	PLA23
LAMOST J110901.22+075441.8	4440	0.70	1.98	−3.41	−2.25	+1.16	−0.85	−0.57	+0.41	Halo	LIH15
BPS CS 22885-096	5050	2.00	1.80	−3.60	−2.60	+1.00	−1.74	⋯	+0.26	Halo	RYA96
SMSS J024858.41-684306.4	4977	1.60	1.80	−3.71	−2.71	+1.00	−0.41	+0.66	+0.57	Halo	JAC15

Notes.
[a] The Fornax dwarf galaxy.
[b] The Ursa Minor dwarf galaxy.
[c] The Reticulum II dwarf galaxy.
[d] The M15 globular cluster.

References. RYA96: Ryan et al. (1996); SHE01: Shetrone et al. (2001); SNE03: Sneden et al. (2003); BAR05: Barklem et al. (2005); LAI08: Lai et al. (2008); HAY09: Hayek et al. (2009); AOK10: Aoki et al. (2010); ALL12: Allen et al. (2012); COH13: Cohen et al. (2013); ROE14: Roederer et al. (2014a); JAC15: Jacobson et al. (2015); LIH15: Li et al. (2015); HOW16: Howes et al. (2016); JI16: Ji et al. (2016); PLA17: Placco et al. (2017); HAN18: Hansen et al. (2018); HAW18: Hawkins & Wyse (2018); ROE18: Roederer et al. (2018b); SAK18: Sakari et al. (2018); XIN19: Xing et al. (2019); CAI20: Cain et al. (2020); EZZ20: Ezzeddine et al. (2020); HOL20: Holmbeck et al. (2020); RAS20: Rasmussen et al. (2020); GUL21: Gull et al. (2021); REI21: Reichert et al. (2021); PLA23: Placco et al. (2023); GAR24: Cabrera Garcia et al. (2024); ROE24: Roederer et al. (2024); SHA24: Shah et al. (2024).

ORCID iDs

Xiao-Jin Xie https://orcid.org/0000-0002-4440-4803
Jianrong Shi https://orcid.org/0000-0002-0349-7839
Hong-Liang Yan https://orcid.org/0000-0002-8609-3599
Tian-Yi Chen https://orcid.org/0000-0002-6448-8995
Carlos Allende Prieto https://orcid.org/0000-0002-0084-572X

Timothy C. Beers https://orcid.org/0000-0003-4573-6233
Shuai Liu https://orcid.org/0000-0001-5193-1727
Chun-Qian Li https://orcid.org/0000-0002-6647-3957
Ming-Yi Ding https://orcid.org/0000-0001-6898-7620
Yao-Jia Tang https://orcid.org/0009-0006-3386-4632
Ruizhi Zhang https://orcid.org/0009-0008-1319-1084
Renjing Xie https://orcid.org/0009-0002-4282-668X

References

Abbott, B. P., Abbott, R., Abbott, T. D., et al. 2017, PhRvL, 119, 161101
Allen, D. M., Ryan, S. G., Rossi, S., Beers, T. C., & Tsangarides, S. A. 2012, A&A, 548, A34
Allende Prieto, C. 2021, NatAs, 5, 105
Alonso, A., Arribas, S., & Martínez-Roger, C. 1999, A&AS, 140, 261
Amôres, E. B., Jesus, R. M., Moitinho, A., et al. 2021, MNRAS, 508, 1788
Aoki, M., Ishimaru, Y., Aoki, W., & Wanajo, S. 2017, ApJ, 837, 8
Aoki, W., Beers, T. C., Honda, S., & Carollo, D. 2010, ApJL, 723, L201
Asplund, M., Grevesse, N., Sauval, A. J., & Scott, P. 2009, ARA&A, 47, 481
Bailer-Jones, C. A. L., Rybizki, J., Fouesneau, M., Demleitner, M., & Andrae, R. 2021, AJ, 161, 147
Barklem, P. S., Christlieb, N., Beers, T. C., et al. 2005, A&A, 439, 129
Battistini, C., & Bensby, T. 2015, A&A, 577, A9
Battistini, C., & Bensby, T. 2016, A&A, 586, A49
Baumueller, D., & Gehren, T. 1996, A&A, 307, 961
Beers, T. C., & Christlieb, N. 2005, ARA&A, 43, 531
Bennett, M., & Bovy, J. 2019, MNRAS, 482, 1417
Bensby, T., Feltzing, S., & Lundström, I. 2003, A&A, 410, 527
Bensby, T., Feltzing, S., & Oey, M. S. 2014, A&A, 562, A71
Blanco-Cuaresma, S., Soubiran, C., Jofré, P., & Heiter, U. 2014, A&A, 566, A98
Borghs, G., de Bisschop, P., van Hove, M., & Silverans, R. E. 1983, HyInt, 15, 177
Brauer, K., Ji, A. P., Drout, M. R., & Frebel, A. 2021, ApJ, 915, 81
Cabrera Garcia, J., Sakari, C. M., Roederer, I. U., et al. 2024, ApJ, 967, 101
Cain, M., Frebel, A., Ji, A. P., et al. 2020, ApJ, 898, 40
Cayrel, R., Hill, V., Beers, T. C., et al. 2001, Natur, 409, 691
Chen, T.-Y., Shi, J.-R., Beers, T. C., et al. 2021, RAA, 21, 036
Cohen, J. G., Christlieb, N., Thompson, I., et al. 2013, ApJ, 778, 56
Côté, B., Eichler, M., Arcones, A., et al. 2019, ApJ, 875, 106
Côté, B., Fryer, C. L., Belczynski, K., et al. 2018, ApJ, 855, 99
Cui, X.-Q., Zhao, Y.-H., Chu, Y.-Q., et al. 2012, RAA, 12, 1197
da Silva, L., Girardi, L., Pasquini, L., et al. 2006, A&A, 458, 609
Drout, M. R., Piro, A. L., Shappee, B. J., et al. 2017, Sci, 358, 1570
Ekanger, N., Bhattacharya, M., & Horiuchi, S. 2023, MNRAS, 525, 2040
Ezzeddine, R., Rasmussen, K., Frebel, A., et al. 2020, ApJ, 898, 150
Farouqi, K., Kratz, K. L., Pfeiffer, B., et al. 2010, ApJ, 712, 1359
Farouqi, K., Thielemann, F. –K., Rosswog, S., & Kratz, K. –L. 2022, A&A, 663, A70
Forsberg, R., Jönsson, H., Ryde, N., & Matteucci, F. 2019, A&A, 631, A113
Frebel, A. 2018, ARNPS, 68, 237
Fujimoto, S.-i., Nishimura, N., & Hashimoto, M.-a. 2008, ApJ, 680, 1350
Gaia Collaboration, Vallenari, A., Brown, A. G. A., et al. 2023, A&A, 674, A1
Gehren, T., Liang, Y. C., Shi, J. R., Zhang, H. W., & Zhao, G. 2004, A&A, 413, 1045
Green, G. M., Schlafly, E., Zucker, C., Speagle, J. S., & Finkbeiner, D. 2019, ApJ, 887, 93
Grichener, Aldana, & Soker, Noam 2019, ApJ, 878, 24
Gull, M., Frebel, A., Hinojosa, K., et al. 2021, ApJ, 912, 52
Gustafsson, B., Edvardsson, B., Eriksson, K., et al. 2008, A&A, 486, 951
Hansen, T. T., Holmbeck, E. M., Beers, T. C., et al. 2018, ApJ, 858, 92
Hattori, K., Okuno, A., & Roederer, I. U. 2023, ApJ, 946, 48
Hawkins, K., & Wyse, R. F. G. 2018, MNRAS, 481, 1028
Hayek, W., Wiesendahl, U., Christlieb, N., et al. 2009, A&A, 504, 511
Hirai, Y., Beers, T. C., Chiba, M., et al. 2022, MNRAS, 517, 4856
Hirai, Y., Ishimaru, Y., Saitoh, T. R., et al. 2015, ApJ, 814, 41
Holmbeck, E. M., Hansen, T. T., Beers, T. C., et al. 2020, ApJS, 249, 30
Hotokezaka, K., Beniamini, P., & Piran, T. 2018, IJMPD, 27, 1842005
Howes, L. M., Asplund, M., Keller, S. C., et al. 2016, MNRAS, 460, 884
Jacobson, H. R., Keller, S., Frebel, A., et al. 2015, ApJ, 807, 171
Jeon, M., Besla, G., & Bromm, V. 2021, MNRAS, 506, 1850
Ji, A. P., Frebel, A., Chiti, A., & Simon, J. D. 2016, Natur, 531, 610
Jin, Shilun, & Soker, Noam 2023, arXiv:2310.08907
Kasen, D., Metzger, B., Barnes, J., Quataert, E., & Ramirez-Ruiz, E. 2017, Natur, 551, 80
Kobayashi, C., Mandel, I., Belczynski, K., et al. 2023, ApJL, 943, L12
Kovalev, M. 2019, PhD thesis, Univ. Heidelberg doi:10.11588/heidok.00027411
Kurucz, R. L., & Bell, B. 1995, Atomic Line List, Kurucz CD-ROM (Cambridge, MA: Smithsonian Astrophysical Observatory)
Kurucz, R. L., Furenlid, I., Brault, J., & Testerman, L. 1984, National Solar Observatory Atlas, sunspot, New Mexico: National Solar Observatory (Sunspot, NM: National Solar Observatory)
Lai, D. K., Bolte, M., Johnson, J. A., et al. 2008, ApJ, 681, 1524
Lattimer, J. M., & Schramm, D. N. 1974, ApJL, 192, L145
Lawler, J. E., Wickliffe, M. E., den Hartog, E. A., & Sneden, C. 2001, ApJ, 563, 1075
Li, H.-N., Aoki, W., Honda, S., et al. 2015, RAA, 15, 1264
Lindegren, L., Bastian, U., Biermann, M., et al. 2021, A&A, 649, A4
Liu, C., Fu, J., Shi, J., et al. 2020, arXiv:2005.07210
Luo, A. L., Zhao, Y. H., Zhao, G., et al. 2022, VizieR On-line Data Catalog, V/156
Mashonkina, L. 2013, A&A, 550, A28
Mashonkina, L., & Gehren, T. 2000, A&A, 364, 249
Mashonkina, L., Gehren, T., & Bikmaev, I. 1999, A&A, 343, 519
Mashonkina, L., Gehren, T., Shi, J. R., Korn, A. J., & Grupp, F. 2011, A&A, 528, A87
Mashonkina, L., Korn, A. J., & Przybilla, N. 2007, A&A, 461, 261
Masseron, T., Plez, B., Van Eck, S., et al. 2014, A&A, 571, A47
Matsuno, T., Hirai, Y., Tarumi, Y., et al. 2021, A&A, 650, A110
McMillan, P. J. 2017, MNRAS, 465, 76
McWilliam, A., Preston, G. W., Sneden, C., & Searle, L. 1995, AJ, 109, 2757
Mirizzi, A. 2015, PhRvD, 92, 105020
Naidu, R. P., Conroy, C., Bonaca, A., et al. 2020, ApJ, 901, 48
Naidu, R. P., Ji, A. P., Conroy, C., et al. 2022, ApJL, 926, L36
Nishimura, N., Takiwaki, T., & Thielemann, F.-K. 2015, ApJ, 810, 109
Obergaulinger, M., Just, O., & Aloy, M. A. 2018, JPhG, 45, 084001
Pian, E., D'Avanzo, P., Benetti, S., et al. 2017, Natur, 551, 67
Placco, V. M., Almeida-Fernandes, F., Holmbeck, E. M., et al. 2023, ApJ, 959, 60
Placco, V. M., Frebel, A., Beers, T. C., & Stancliffe, R. J. 2014, ApJ, 797, 21
Placco, V. M., Holmbeck, E. M., Frebel, A., et al. 2017, ApJ, 844, 18
Ramírez, I., & Meléndez, J. 2005, ApJ, 626, 465
Rasmussen, K. C., Zepeda, J., Beers, T. C., et al. 2020, ApJ, 905, 20
Reetz, J. K. 1999, PhD thesis, Ludwig-Maximilians Univ. of Munich, Germany
Reichert, M., Hansen, C. J., & Arcones, A. 2021, ApJ, 912, 157
Reichert, M., Obergaulinger, M., Aloy, M. Á., et al. 2023, MNRAS, 518, 1557
Roederer, I. U., Beers, T. C., Hattori, K., et al. 2024, arXiv:2406.02691
Roederer, I. U., Cowan, J. J., Pignatari, M., et al. 2022a, ApJ, 936, 84
Roederer, I. U., Cowan, J. J., Preston, G. W., et al. 2014a, MNRAS, 445, 2970
Roederer, I. U., Hattori, K., & Valluri, M. 2018a, AJ, 156, 179
Roederer, I. U., Lawler, J. E., Den Hartog, E. A., et al. 2022b, ApJS, 260, 27
Roederer, I. U., Preston, G. W., Thompson, I. B., et al. 2014b, AJ, 147, 136
Roederer, I. U., Sakari, C. M., Placco, V. M., et al. 2018b, ApJ, 865, 129
Rosswog, S., Korobkin, O., Arcones, A., Thielemann, F. K., & Piran, T. 2014, MNRAS, 439, 744
Ryan, S. G., Norris, J. E., & Beers, T. C. 1996, ApJ, 471, 254
Sakari, C. M., Placco, V. M., Farrell, E. M., et al. 2018, ApJ, 868, 110
Sakari, C. M., Roederer, I. U., Placco, V. M., et al. 2019, ApJ, 874, 148
Sato, K. 1974, PThPh, 51, 726
Schatz, H., Toenjes, R., Pfeiffer, B., et al. 2002, ApJ, 579, 626
Schönrich, R., Binney, J., & Dehnen, W. 2010, MNRAS, 403, 1829
Shah, S. P., Ezzeddine, R., Roederer, I. U., et al. 2024, MNRAS, 529, 1917
Shank, D., Beers, T. C., Placco, V. M., et al. 2023, ApJ, 943, 23
Shetrone, M. D., Côté, P., & Sargent, W. L. W. 2001, ApJ, 548, 592
Shi, J. R., Gehren, T., Butler, K., Mashonkina, L. I., & Zhao, G. 2008, A&A, 486, 303
Shi, J. R., Gehren, T., Zeng, J. L., Mashonkina, L., & Zhao, G. 2014, ApJ, 782, 80
Siegel, D. M. 2019, EPJA, 55, 203
Siegel, D. M., Barnes, J., & Metzger, B. D. 2019, Natur, 569, 241
Sitnova, T., Zhao, G., Mashonkina, L., et al. 2015, ApJ, 808, 148
Sitnova, T. M., Mashonkina, L. I., & Ryabchikova, T. A. 2016, MNRAS, 461, 1000
Sneden, C., Cowan, J. J., & Gallino, R. 2008, ARA&A, 46, 241
Sneden, C., Cowan, J. J., Lawler, J. E., et al. 2003, ApJ, 591, 936
Sneden, C., Preston, G. W., McWilliam, A., & Searle, L. 1994, ApJL, 431, L27

Stoehr, F., White, R., Smith, M., et al. 2008, in ASP Conf. Ser. 394, Astronomical Data Analysis Software and Systems XVII, ed. R. W. Argyle, P. S. Bunclark, & J. R. Lewis (San Francisco, CA: ASP), 505
Symbalisty, E. M. D., Schramm, D. N., & Wilson, J. R. 1985, ApJL, 291, L11
Tabernero, H. M., Allende Prieto, C., Zapatero Osorio, M. R., et al. 2020, MNRAS, 498, 4222
Thielemann, F. K., Eichler, M., Panov, I. V., & Wehmeyer, B. 2017, ARNPS, 67, 253
Tsujimoto, T. 2021, ApJL, 920, L32
Vasiliev, E. 2019, MNRAS, 482, 1525
Venn, K. A., Irwin, M., Shetrone, M. D., et al. 2004, AJ, 128, 1177
Watson, D., Hansen, C. J., Selsing, J., et al. 2019, Natur, 574, 497
Witti, J., Janka, H. T., & Takahashi, K. 1994, A&A, 286, 841
Xing, Q.-F., Zhao, G., Aoki, W., et al. 2019, NatAs, 3, 631
Yamazaki, Y., Kajino, T., Mathews, G. J., et al. 2021, arXiv:2102.05891
Yan, H., Li, H., Wang, S., et al. 2022, Innov, 3, 100224
Yan, H.-L., Shi, J.-R., Zhou, Y.-T., et al. 2018, NatAs, 2, 790
Zacharias, N., Finch, C. T., Girard, T. M., et al. 2013, AJ, 145, 44
Zhang, H. W., Gehren, T., & Zhao, G. 2008, A&A, 481, 489
Zhao, G., Mashonkina, L., Yan, H. L., et al. 2016, ApJ, 833, 225
Zhao, G., Zhao, Y.-H., Chu, Y.-Q., Jing, Y.-P., & Deng, L.-C. 2012, RAA, 12, 723